Northumbria
University
NEWCASTLE

ACS APPLIED ENERGY MATERIALS

Letter

Cite This: ACS Appl. Energy Mater. 2020, 3, 122−128

www.acsaem.org

Real-Time Electron Nanoscopy of Photovoltaic Absorber Formation from Kesterite Nanoparticles

Yongtao Qu,[†] See Wee Chee,[‡,§] Martial Duchamp,[∥] Stephen Campbell,[†] Guillaume Zoppi,[†] Vincent Barrioz,[†] Yvelin Giret,[⊥] Thomas J. Penfold,[⊥] Apoorva Chaturvedi,[∥] Utkur Mirsaidov,[‡,§] and Neil S. Beattie*[,†]

[†]Department of Mathematics, Physics and Electrical Engineering, Northumbria University, Newcastle upon Tyne NE1 8ST, United Kingdom

[‡]Department of Physics, National University of Singapore, 117551, Singapore

[§]Centre for BioImaging Sciences, Department of Biological Sciences, National University of Singapore, 117557, Singapore

[∥]Laboratory for In Situ and Operando Electron Nanoscopy, School of Materials Science and Engineering, Nanyang Technological University, 637371, Singapore

[⊥]Chemistry—School of Natural and Environmental Sciences, Newcastle University, Newcastle upon Tyne NE1 7RU, United Kingdom

Supporting Information

ABSTRACT: Cu_2ZnSnS_4 nanocrystals are annealed in a Se-rich atmosphere inside a transmission electron microscope. During the heating phase, a complete S−Se exchange reaction occurs while the cation sublattice and morphology of the nanocrystals are preserved. At the annealing temperature, growth of large $Cu_2ZnSnSe_4$ grains with increased cation ordering is observed in real-time. This yields an annealing protocol which is transferred to an industrially similar solar cell fabrication process resulting in a 33% increase in the device open circuit voltage. The approach can be applied to improve the performance of any photovoltaic technology that requires annealing because of the criticality of the process step.

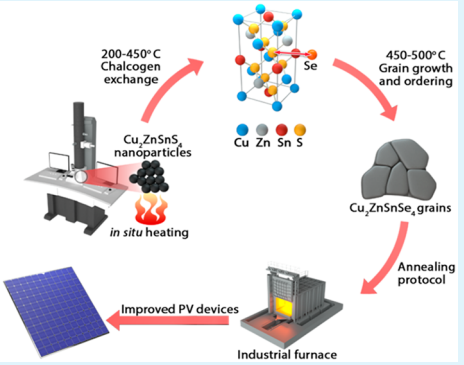

KEYWORDS: *kesterite, photovoltaics, in situ transmission electron microscopy (TEM), annealing, cation ordering*

The current energy challenge facing our society is exemplified in Shell's Sky scenario which projects that global electricity generation by 2070 will be nearly 5 times greater than today's level.[1] This increased capacity will be driven, in part, by the proliferation of new and distributed applications in healthcare, transportation, construction, aerospace, and consumer devices. The growth in these applications defines a new era for photovoltaics because of the demand for innovative and sustainable power sources that can be easily integrated with high value products. This creates a significant opportunity for inorganic thin film photovoltaics because of their stability and compatibility with a variety of flexible substrates including foils, plastics, and ultrathin glass.[2]

The most commercialized thin film technologies are CdTe and $CuInGa(S,Se)_2$ (CIGS) and have efficiencies of >20%.[3] Another chalcogenide material that is closely related to CIGS, but with an increased Earth abundance of the constituent elements, is Cu_2ZnSnS_4 (CZTS). However, CZTS is not yet commercialized because of the challenge associated with achieving sufficiently high open circuit voltage V_{oc}, under illumination, which is essential for high efficiency. This issue is generally associated with disorder in the kesterite crystal lattice resulting in the formation of performance-limiting defect levels.[4,5] Nevertheless, both CZTS and CIGS have the added benefit of solution-based fabrication via nanoparticle inks[6,7] which are compatible with high volume, high value manufacturing. There is therefore an urgent need to understand the formation of the light absorbing layer and associated defects, prepared from nanoparticle inks.

A critically important step to achieve high performance in the fabrication of all thin film photovoltaic absorbers, including CZTS, is an annealing step performed at high temperature. For industrially manufactured devices, the solar absorber layers are annealed in a large-scale furnace with a specific gas atmosphere. This promotes the formation of an absorber with a granular morphology in which the grains are as large as possible to maximize the absorption of photons and grain boundaries are minimized[8,9] or passivated to reduce non-

Received: September 4, 2019
Accepted: December 12, 2019
Published: December 12, 2019

DOI: 10.1021/acsaem.9b01732
ACS Appl. Energy Mater. 2020, 3, 122−128

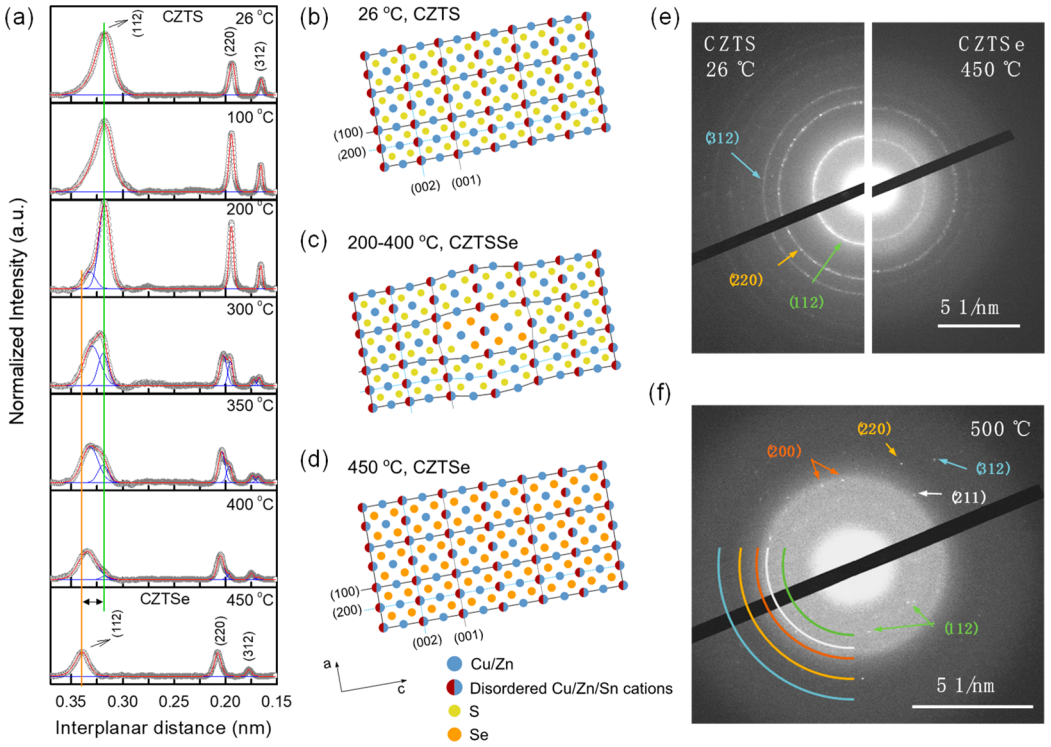

Figure 1. (a) Normalized electron diffraction radial profiles in the temperature range 26−450 °C. Multipeak fits (single peaks, blue solid lines; sum of peaks, red solid line) are applied to identify overlapping diffraction rings. The vertical green line marks the constant position of the CZTS (112) diffraction ring across the chalcogen atom exchange process. The vertical orange line indicates the continuous evolution of CZTSSe (112) reflections with respect to the final position of CZTSe (112) at 450 °C. (b−d) Schematic projection of CZTS/CZTSe crystal structures along the [010] zone axis. (e) Diffraction pattern comparison of as-synthesized CZTS at 26 °C and fully selenized CZTSe at 450 °C. (f) Discrete diffraction spots of CZTSe at 500 °C.

radiative recombination of photogenerated charge carriers.[10,11] Recently, this process has been studied using *in situ* X-ray diffraction;[12−14] however, all these studies were performed on bulk films prepared from stacked nanocrystals. Consequently, the information obtained is averaged over length scales that are much larger than the characteristic dimensions of the nanocrystal itself. This may introduce significant variations in sample properties, such as surface area to volume ratio and reaction rate.

In this work, we thermally anneal CZTS nanoparticle inks in a Se-rich atmosphere in an environmental cell nanoreactor rather than a conventional large-scale furnace and use *in situ* transmission electron microscopy (TEM) to study the formation of $Cu_2ZnSnSe_4$ light absorbing grains directly at the characteristic scale of CZTS nanoparticles and in real-time. On the basis of insights from these results, we develop an annealing protocol which promotes cation ordering. Moreover, we apply this protocol to an industrially similar solar cell fabrication process to create solar cell devices with substantially increased V_{oc}. Significantly, the approach is applicable to any photovoltaic technology that requires thermal annealing to achieve high performance.

A CZTS nanoparticle ink was fabricated by a hot injection method[15] and then applied to a Si-based MEMS chip via spin-coating for *in situ* characterization inside a TEM. A second blank chip was sealed face down to the spin-coated chip to form a nanoreactor with electron transparent windows (Figure S1) to allow *in situ* investigation of thermal annealing of kesterite nanoparticles inside the TEM. A thin film of Se was thermally evaporated on top of the nanoparticles to provide a reactive Se atmosphere during annealing. Before placing the sample inside the TEM, the nanoreactor was sealed in N_2 at 1 atm. To dynamically monitor the chemical and crystal structure changes of the nanoparticles during annealing, a series of selected-area electron diffraction (SAED) patterns were recorded at temperatures from 26 to 700 °C (see Figure S2). To discriminate partially overlapping diffraction rings, the diffraction patterns were converted into normalized radial profiles using ImageJ software.[16] From these data, the signal profiles, positions, and intensities were extracted using a multipeak fit as shown in Figure 1a (peak details are summarized in Table S1).

In the low temperature range, 26−200 °C, the experimental data are in good agreement with tetragonal CZTS (PDF 026-0575). Additionally, as the temperature increases, the diffraction peaks become sharper and more intense indicating increased crystallinity.[17,18] As the temperature approaches the melting point of Se (225 °C), the Se layer becomes thinner (as shown in Figure S3), initiating the S−Se exchange reaction. As shown in Figure 1a, a shoulder in the signal belonging to the (112) reflection of $Cu_2ZnSn(S_{1-x}Se_x)_4$ (CZTSSe) appears at 200 °C, indicating that the incorporation of Se into the CZTS lattice has already started. When the temperature reaches 300 °C, Figure 1a indicates that the diffraction pattern can be indexed to a growing CZTSSe phase and the parent CZTS phase. This is schematically illustrated by the change in the parent lattice from Figure 1b to Figure 1c whereby S atoms in CZTS nanoparticles are replaced by larger Se atoms, resulting in increased interplanar lattice separation.

DOI: 10.1021/acsaem.9b01732
ACS Appl. Energy Mater. 2020, 3, 122−128

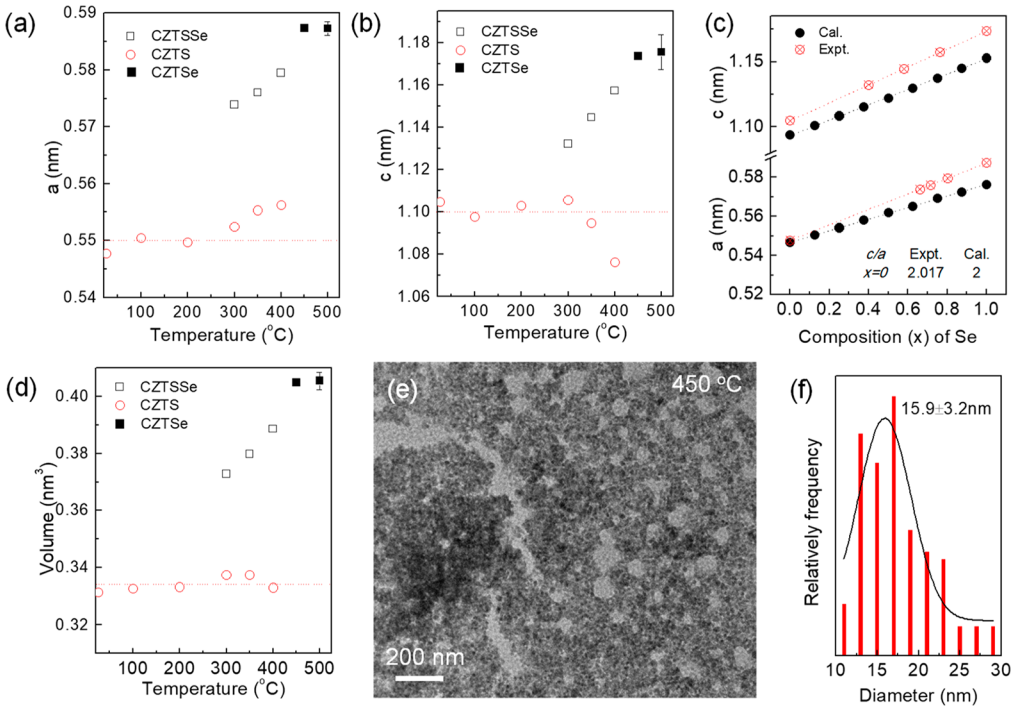

Figure 2. (a, b) Evolution of the lattice constants, *a* and *c*, in the temperature range 26−500 °C. (c) Calculated lattice constants *a* and *c* as a function of Se concentration *x* compared with the experimental data. (d) The unit cell volume expansion as a function of temperature. (e) TEM frame captured at 450 °C. (f) Size distributions of CZTSe nanoparticles at 450 °C. The histogram is fitted with a Gaussian.

By 450 °C (Figure 1a) the diffraction signal matches that of tetragonal CZTSe (PDF 052-0868) indicating that the S−Se exchange reaction is complete and the sample is fully selenized, as shown schematically in Figure 1d. For an additional view of this change, Figure 1e compares the SAED diffraction rings at the extremities of the temperature range in Figure 1a. Notably, the relative intensity of the signal at 450 °C has decreased, implying that sample crystallinity has degraded during the S−Se exchange process. This is due to an increased density of crystallographic boundaries within an individual CZTS nanoparticle during the S−Se exchange process which yields smaller crystalline domains and decreased crystallinity in CZTSe nanoparticles (see Figure S4 for detailed explanation).

It is generally accepted that for CZTS, Cu and Zn atoms are highly disordered[19,20] resulting in antisite defects; however, their impact on solar cell performance has been found to be somewhat limited.[4] Sn-related disorder on the other hand has been found to be more detrimental[5] and has recently been observed with atomic-scale resolution in $Ag_2ZnSnSe_4$.[21] Further randomization of the cations resulted in CZTS nanocrystals with cubic structure at the nanocrystal surface.[22] These led to Sn-related deep level antisite defects which ultimately reduce solar cell performance but also damage the tetragonal symmetry of fully ordered kesterite CZTS. As a result, tetragonal diffraction reflections such as (101), (103), and (211) are absent in the temperature 26−450 °C.

When the annealing temperature reaches 500 °C, the continuous diffraction rings disappear and discrete diffraction spots are visible in the SAED image in Figure 1f, implying significant crystal growth. The spots stem from reflections of pure CZTSe as emphasized by the colored curves in Figure 1f. Compared with the previous patterns, more diffraction planes can be observed due to the better crystallinity developed in this stage. Interestingly, previously absent diffraction spots from (211) reflections are now weakly visible and highlighted by the white curve. This implies increased cation ordering within the CZTSe crystal. We suggest that initial Sn-related disordering in the parent nanoparticles is significantly reduced during the recrystallization and grain growth process. This hypothesis is supported by two pieces of additional experimental evidence. First, the CZTSe grains approach stoichiometry compared to the as deposited CZTS nanoparticles (seen in Table S2). This follows from a zinc loss during the selenization process, which implies that less Zn is available to occupy Sn sites (the 2*b* Wyckoff positions[19]). Second, our deep level transient spectroscopy (DLTS) data[23] shows that the deep level Zn_{Sn} antisite defect has been passivated in the large grained CZTSe thin film. Increased Sn ordering would allow the CZTSe to possess an ordered tetragonal unit cell, resulting in the rise of the (211) reflection after selenization.

At 600 °C (see Figure S2) the diffraction spots decay significantly, and the pattern can be indexed to cubic $CuSe_2$ (PDF 01-071-0047). This is likely to be due to the decomposition of CZTSe at high temperature.[24,25] When the temperature is further increased to 700 °C, no diffraction pattern is observed (seen in Figure S2), implying that the sample has completely decomposed and transited to an amorphous state.

Notably in Figure 1a, the position of the parent CZTS diffraction peaks remains constant over a relatively wide temperature range as indicated by the vertical green line. As a result, the CZTS lattice constants (i.e., $a \sim 0.55$ nm and $c \sim 1.10$ nm) are stable in this range as shown in Figure 2a,b. Therefore, although consumed by the growing CZTSSe phase, the parent CZTS phase is structurally stable during the S−Se exchange process. In contrast, however, the CZTSSe lattice constant *a* increased from ~0.57 to ~0.58 nm, and *c* increased

DOI: 10.1021/acsaem.9b01732
ACS Appl. Energy Mater. 2020, 3, 122−128

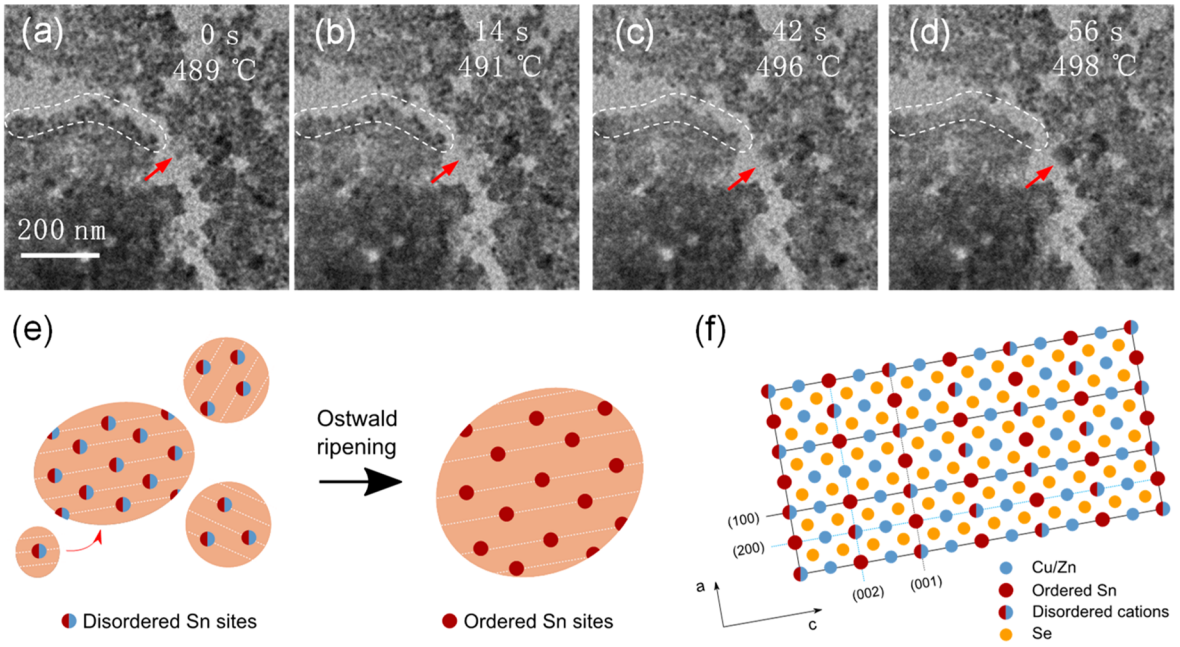

Figure 3. Growth dynamics of the CZTSe grains from 489 to 498 °C: (a) 0 s, 489 °C; (b) 14 s, 491 °C; (c) 42 s, 496 °C; (d) 56 s, 498 °C. Time listed in figures is relative to the first frame. Scale bar in part a also applies to parts b–d. (e) Schematic representation of the grain growth stage included in parts a–d. The white dashed lines illustrate the various crystal orientations of nanoparticles. The large particle in the middle grows upon sacrifice of small particles nearby and becomes even larger. (f) CZTSe crystal structure with ordered Sn sites developed in the grain growth stage.

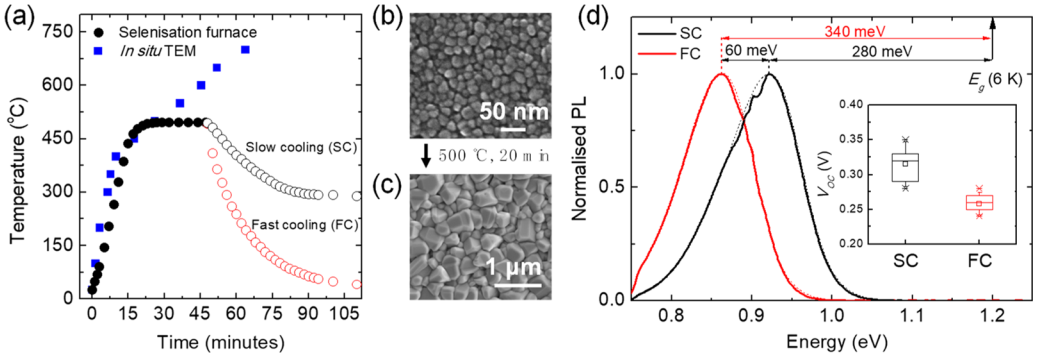

Figure 4. (a) Temperature profiles of the TEM and selenization experiments. Open circles (○) indicate different cooling profiles in the selenization experiment. Top view SEM images showing (b) a CZTS nanoparticle thin film before selenization and (c) the output film morphology following selenization. (d) PL spectra of slow-cooled (SC) and fast-cooled (FC) CZTSSe thin films at 6 K and the same excitation intensity. The dashed line is an asymmetric double sigmoidal curve fit used to evaluate the peak of each PL band. The feature apparent around 0.9 eV is due to light absorption by water vapor. The inset shows the V_{oc} of the solar cells made from SC and FC absorbers, respectively. □ is the average value. × symbols represent the minimum and maximum positions. The three horizontal lines of each box stand for the 25%, 50%, and 75% of the reading distribution. The whisker range is determined by the standard deviation of the 15 devices.

from ~1.13 to ~1.17 nm in the range 300–450 °C as shown in Figure 2a,b.

To further investigate the unit cell evolution introduced by the chalcogen atom exchange, we calculated the evolution of the lattice constants *a* and *c* as a function of Se concentration *x* for ordered tetragonal, i.e., kesterite $Cu_2ZnSn(S_{1-x}Se_x)_4$ as shown in Figure 2c (see SI for the detailed computational design). From Vegard's law, the gradient of a linear fit to the evolution of the lattice constants with composition yields the lattice mismatch between CZTS and CZTSe.[26] Differences between the gradients obtained for *a* and *c* indicate an uneven unit cell expansion driven by cation disorder, especially along the *c*-axis.[27] As a result, an increased *c*/*a* ratio (values given in inset to Figure 2c) is expected for disordered CZTS nanoparticles compared with the model.

As expected, the parent CZTS phase has no significant unit cell volume change while the S–Se exchange reaction introduces a unit cell volume expansion up to ~20% for the growing CZTSSe phase as shown in Figure 2d. The TEM frame at 450 °C (captured in Figure 2e) shows monodispersed CZTSe nanoparticles after S–Se exchange with an average particle size of 15.9 nm. By comparison, the initial CZTS nanoparticles at 26 °C have an average size of 13.3 nm (for *ex situ* TEM micrograph, see Figure S5). This unit cell expansion can be fully explained by the replacement of S by Se, which is confirmed by the comparison with the calculations shown in Figure 2c. Despite this volume expansion, the shape and characteristic length scale of the initial CZTS nanoparticles is preserved during the phase transition as neighboring nanoparticles did not coalesce or merge into larger grains.

DOI: 10.1021/acsaem.9b01732
ACS Appl. Energy Mater. 2020, 3, 122–128

Above 450 °C, we observed the formation of large-sized CZTSe grains in real-time in the TEM. The dynamics of CZTSe grain growth in the temperature range from 480 to 500 °C are recorded in Video 1. The snapshot frames captured are shown in Figure 3a–d, and as shown in Figure 3a, the nanoparticle indicated by the red arrow is measured to have a lateral size of ∼20 nm, which is slightly larger than the average particle size of CZTSe. As the temperature increases, the nanoparticle diameter increases to ∼50 nm at 496 °C, together with the nanoparticles enclosed by the white dashed line becoming smaller and blurred. When the temperature reaches 498 °C in less than 1 min, the lateral size of CZTSe grains has been enlarged three times while the nanoparticles enclosed by the dashed line disappear (see in Figure 3d and Video 1). This behavior is consistent with Ostwald ripening[28] schematically illustrated in Figure 3e where CZTSe large grains with limited orientations grow bigger by consuming small grains with different crystallographic orientations. This model accounts for the emergence of discrete diffraction spots observed in Figure 1f. Moreover, the rise of the weak (211) reflection of the tetragonal structure around this temperature implies that the initially disordered Sn sites on (002) and (001) planes can be significantly reduced during the recrystallization and grain growth process. The increased structural order associated with the tetragonal symmetry is shown schematically in Figure 3f.

Our *in situ* TEM experiments reveal the new insight that chalcogen atom exchange and grain growth are distinct and separate processes. Furthermore, the grain growth is accompanied by an improvement in the crystallinity of the material and cation ordering within the kesterite structure. To promote this ordering and reduce the density of defects in a CZTS thin film photovoltaic absorber, we transferred the insights obtained from the *in situ* TEM experiment to a photovoltaic device fabrication step that more closely resembles an industrial process. This involved creating CZTSe thin film photovoltaic absorbers in a selenization furnace (see SI for details). To distinguish this experiment from the *in situ* TEM, we refer to it as selenization, and a comparison of the heating profiles in each may be found in Figure 4a, where it can be seen that the heating rates between the TEM and selenization experiments are very similar.

The top-view scanning electron microscope image in Figure 4b shows a uniform thin film of CZTS nanoparticles before selenization. On the basis of the insights from the *in situ* TEM experiment, an annealing temperature of 500 °C was maintained in the selenization furnace for ∼20 min before being cooled to room temperature. A slow-cooling (SC) temperature profile was used to maximize the cation ordering and grain growth observed in the TEM, and for comparison, a fast-cooling (FC) profile was also performed on a different sample. In both SC and FC, a representative sample morphology following the selenization experiment is shown in Figure 4c, and it can be seen that the thin film morphology has transitioned from nanoparticles to smooth, micrometer-sized grains.

In order to assess the impact of the relative cooling rate on the selenized thin films, a low temperature photoluminescence (PL) experiment was performed, and the data are shown in Figure 4d. Both samples show a similar broad, asymmetric PL signal indicative of a semiconductor material with large defect densities which cause electrostatic potential fluctuations in the conduction and valence bands.[29] The PL spectra in Figure 4d are shown relative to the 6 K bandgap energy, and the significant red-shift for both samples is further evidence of defect clusters within both films.

In our recent work[23,30] we have shown that donor/acceptor defect states have low thermal activation energies in contrast to the large red-shift of the PL bands from the bandgap energy of CZTSSe films, indicating the presence of deep defects. Tiwari et al. have shown such behavior results from recombination related to defect clusters that lead to a narrowing of the absorber bandgap.[31] The defect cluster [$2Cu_{Zn}$ + Sn_{Zn}], which is caused by both Cu–Zn and Sn–Zn disorder, was found to induce a large bandgap decrease of 350 meV and results in spatial bandgap fluctuations within the absorber.[32] The magnitude of the red-shift in the FC film in Figure 4d could be attributed to this defect cluster. In the SC sample, however, this red-shift is notably 60 meV smaller. From power-dependence measurements of the PL (see Figure S6) the ratio of the radiative to total defect concentrations was determined to be 0.12 and 0.10 for the SC and FC samples, respectively. Therefore, given that the SC absorber has a lower proportion of nonradiative defects, including the electron-trapping Sn_{Zn} deep defect, we conclude that slower cooling results in increased crystallographic order.

To further assess the impact of improved crystallinity and grain growth observed in the TEM, both SC and FC thin film photovoltaic absorbers were integrated into a conventional thin film solar cell device architecture (details given in SI). The inset to Figure 4d shows an average increase in open circuit voltage (V_{oc}) of ∼50 meV for the SC absorbers across 15 devices with the best efficiency of ∼7% without optimization of the other device parameters (see Figure S7), demonstrating a feasible route to improving device performance in kesterite solar cells.

In summary, CZTS earth-abundant nanoparticles were annealed in a Se-rich atmosphere for the first time in a TEM. This revealed the chalcogen atom exchange and grain growth processes to be distinct and occurring within different temperature ranges. A further observation was the improved crystallinity at a temperature within a typical range used for industrial fabrication of thin film chalcogenide solar cells. The insights obtained at the nanometer scale in the TEM were subsequently exploited to increase the open circuit voltage of kesterite solar cells via reduction of cation disorder. These experiments demonstrate a new approach to improve the performance of any photovoltaic technology that requires thermal annealing in the device fabrication.

■ ASSOCIATED CONTENT

Supporting Information

The Supporting Information is available free of charge at https://pubs.acs.org/doi/10.1021/acsaem.9b01732.

Experimental details and following additional data: side-view schematic of the gas cell for the *in situ* TEM study; the full SAED survey from 26 to 700 °C; peak details extracted from the radial profiles in Figure 1a; TEM images captured at 26, 100, and 200 °C; the composition of as-deposited CZTS nanoparticle and selenized thin film; crystal structures of CZTS; the *ex situ* TEM micrograph and elemental map of CZTS nanoparticles; Avrami–Erofeev nucleation and growth model in a single nanoparticle; excitation-dependent PL spectra of SC and FC absorbers; and *JV* curves of the best device in this research series (PDF)

DOI: 10.1021/acsaem.9b01732
ACS Appl. Energy Mater. 2020, 3, 122–128

Video 1 showing the growth dynamics of CZTSe grain on consuming nanoparticles in the temperature range from 488 to 500 °C (AVI)

AUTHOR INFORMATION

Corresponding Author

*E-mail: neil.beattie@northumbria.ac.uk.

ORCID

See Wee Chee: 0000-0003-0095-3242
Guillaume Zoppi: 0000-0003-3622-6899
Utkur Mirsaidov: 0000-0001-8673-466X
Neil S. Beattie: 0000-0002-0098-4420

Author Contributions

Y.Q. developed the CZTS nanoparticles, photovoltaic absorbers, and solar cells. Y.Q., G.Z., M.D., V.B., and N.S.B discussed and planned the annealing and real-time measurements. S.W.C, M.D., and U.M. performed the TEM measurements. A.C. deposited the Se thin film on CZTS nanoparticles. Y.G. and T.J.P. performed the theoretical calculations. S.C. performed the thin film photoluminescence measurements. Y.Q., S.C., G.Z., V.B., and N.S.B. evaluated the real-time measurements, developed the model, and drafted the manuscript. N.S.B supervised this project. All authors discussed the results and contributed to the manuscript modification. All authors have given approval to the final version of the manuscript.

Notes

The authors declare no competing financial interest.

ACKNOWLEDGMENTS

S.W.C. and U.M. acknowledge the funding support from the National Research Foundation of Singapore's Competitive Research Program (NRF-CRP16-2015-05). M.D. acknowledges the financial support from Nanyang Technological University start-up grant M4081924. *Ex situ* electron microscopy imaging was performed at the Facility for Analysis, Characterization, Testing and Simulation (FACTS) in Nanyang Technological University, Singapore. N.S.B, G.Z., and T.J.P. acknowledge the EPSRC for funding through grants EP/R014884/1, EP/N024389/1, and EP/R021503/1 (The North East Centre for Energy Materials). The authors gratefully acknowledge useful discussions about the work with Professor Ken Durose at the University of Liverpool, UK.

REFERENCES

(1) Shell International, B.V. Sky Scenario. www.shell.com/skyscenario.

(2) Polman, A.; Knight, M.; Garnett, E. C.; Ehrler, B.; Sinke, W. C. Photovoltaic Materials: Present Efficiencies and Future Challenges. *Science* **2016**, *352*, aad4424.

(3) Green, M. A.; Hishikawa, Y.; Dunlop, E. D.; Levi, D. H.; Hohl-Ebinger, J.; Yoshita, M.; Ho-Baillie, A. W. Y. Solar Cell Efficiency Tables (Version 53). *Prog. Photovoltaics* **2019**, *27*, 3−12.

(4) Bourdais, S.; Choné, C.; Delatouche, B.; Jacob, A.; Larramona, G.; Moisan, C.; Lafond, A.; Donatini, F.; Rey, G.; Siebentritt, S.; Walsh, A.; Dennler, G. Is the Cu/Zn Disorder the Main Culprit for the Voltage Deficit in Kesterite Solar Cells? *Adv. Energy Mater.* **2016**, *6*, 1502276.

(5) Chen, S.; Walsh, A.; Gong, X.-G.; Wei, S.-H. Classification of Lattice Defects in the Kesterite Cu_2ZnSnS_4 and $Cu_2ZnSnSe_4$ Earth-Abundant Solar Cell Absorbers. *Adv. Mater.* **2013**, *25*, 1522−1539.

(6) Zhou, H.; Hsu, W. C.; Duan, H. S.; Bob, B.; Yang, W.; Song, T. B.; Hsu, C. J.; Yang, Y. CZTS Nanocrystals: A Promising Approach for Next Generation Thin Film Photovoltaics. *Energy Environ. Sci.* **2013**, *6*, 2822−2838.

(7) Guo, Q. J.; Ford, G. M.; Agrawal, R.; Hillhouse, H. W. Ink Formulation and Low-Temperature Incorporation of Sodium to Yield 12% Efficient $Cu(In,Ga)(S,Se)_2$ Solar Cells from Sulfide Nanocrystal Inks. *Prog. Photovoltaics* **2013**, *21*, 64−71.

(8) Wang, W.; Winkler, M. T.; Gunawan, O.; Gokmen, T.; Todorov, T. K.; Zhu, Y.; Mitzi, D. B. Device Characteristics of CZTSSe Thin-Film Solar Cells with 12.6% Efficiency. *Adv. Energy Mater.* **2014**, *4*, 1301465.

(9) Todorov, T. K.; Gunawan, O.; Gokmen, T.; Mitzi, D. B. Solution-Processed $Cu(In,Ga)(S,Se)_2$ Absorber Yielding a 15.2% Efficient Solar Cell. *Prog. Photovoltaics* **2013**, *21*, 82−87.

(10) Major, J. D.; Al Turkestani, M.; Bowen, L.; Brossard, M.; Li, C.; Lagoudakis, P.; Pennycook, S. J.; Phillips, L. J.; Treharne, R. E.; Durose, K. In-Depth Analysis of Chloride Treatments for Thin-Film CdTe Solar Cells. *Nat. Commun.* **2016**, *7*, 13231.

(11) Major, J. D.; Treharne, R. E.; Phillips, L. J.; Durose, K. A Low-Cost Non-Toxic Post-Growth Activation Step for CdTe Solar Cells. *Nature* **2014**, *511*, 334.

(12) Mainz, R.; Singh, A.; Levcenko, S.; Klaus, M.; Genzel, C.; Ryan, K. M.; Unold, T. Phase-Transition-Driven Growth of Compound Semiconductor Crystals from Ordered Metastable Nanorods. *Nat. Commun.* **2014**, *5*, 3133.

(13) Mainz, R.; Walker, B. C.; Schmidt, S. S.; Zander, O.; Weber, A.; Rodriguez-Alvarez, H.; Just, J.; Klaus, M.; Agrawal, R.; Unold, T. Real-Time Observation of $Cu_2ZnSn(S,Se)_4$ Solar Cell Absorber Layer Formation from Nanoparticle Precursors. *Phys. Chem. Chem. Phys.* **2013**, *15*, 18281−18289.

(14) Brandl, M.; Sayed, M. H.; Chory, C.; Hammer-Riedel, I.; Parisi, J.; Hock, R.; Gütay, L. In-Situ XRD Investigation of Selenization of CZTS Nanoparticles. *J. Alloys Compd.* **2017**, *714*, 35−38.

(15) Qu, Y.; Zoppi, G.; Beattie, N. S. The Role of Nanoparticle Inks in Determining the Performance of Solution Processed $Cu_2ZnSn(S,Se)_4$ Thin Film Solar Cells. *Prog. Photovoltaics* **2016**, *24*, 836−845.

(16) Yu, J.; Yuan, W.; Yang, H.; Xu, Q.; Wang, Y.; Zhang, Z. Fast Gas−Solid Reaction Kinetics of Nanoparticles Unveiled by Millisecond in Situ Electron Diffraction at Ambient Pressure. *Angew. Chem., Int. Ed.* **2018**, *57*, 11344−11348.

(17) Kattan, N.; Hou, B.; Fermín, D. J.; Cherns, D. Crystal Structure and Defects Visualization of Cu_2ZnSnS_4 Nanoparticles Employing Transmission Electron Microscopy and Electron Diffraction. *Appl. Mater. Today* **2015**, *1*, 52−59.

(18) Sayed, M. H.; Brandl, M.; Chory, C.; Hammer-Riedel, I.; Parisi, J.; Gütay, L.; Hock, R. In-Situ XRD Investigation of Re-Crystallization and Selenization of CZTS Nanoparticles. *J. Alloys Compd.* **2016**, *686*, 24−29.

(19) Bosson, C. J. *Understanding Cu_2ZnSnS_4 as a Photovoltaic Absorber for the Future of Solar Electricity*; Durham University, 2017.

(20) Wallace, S. K.; Frost, J. M.; Walsh, A. Atomistic Insights into the Order-Disorder Transition in Cu_2ZnSnS_4 Solar Cells from Monte Carlo Simulations. *J. Mater. Chem. A* **2019**, *7*, 312−321.

(21) Cherns, D.; Griffiths, I. J.; Jones, L.; Bishop, D. M.; Lloyd, M. A.; McCandless, B. E. Direct Observation of High Densities of Antisite Defects in $Ag_2ZnSnSe_4$. *ACS Appl. Energy Mater.* **2018**, *1*, 6260−6267.

(22) Kattan, N. A.; Griffiths, I. J.; Cherns, D.; Fermín, D. J. Observation of Antisite Domain Boundaries in Cu_2ZnSnS_4 by Atomic-Resolution Transmission Electron Microscopy. *Nanoscale* **2016**, *8*, 14369−14373.

(23) Campbell, S.; Qu, Y.; Major, J. D.; Lagarde, D.; Labbé, C.; Maiello, P.; Barrioz, V.; Beattie, N. S.; Zoppi, G. Direct Evidence of Causality between Chemical Purity and Band-Edge Potential Fluctuations in Nanoparticle Ink-Based $Cu_2ZnSn(S,Se)_4$ Solar Cells. *J. Phys. D: Appl. Phys.* **2019**, *52*, 135102.

(24) Weber, A.; Mainz, R.; Schock, H. W. On the Sn Loss from Thin Films of the Material System Cu-Zn-Sn-S in High Vacuum. *J. Appl. Phys.* **2010**, *107*, 013516.

DOI: 10.1021/acsaem.9b01732
ACS Appl. Energy Mater. 2020, 3, 122−128

(25) Redinger, A.; Berg, D. M.; Dale, P. J.; Siebentritt, S. The Consequences of Kesterite Equilibria for Efficient Solar Cells. *J. Am. Chem. Soc.* **2011**, *133*, 3320−3323.
(26) Zhao, Z.-Y.; Liu, Q.-L.; Zhao, X. Dft Calculations Study of Structural, Electronic, and Optical Properties of Cu_2 Zn $Sn(S_{1-X}$ $Se_x)_4$ Alloys. *J. Alloys Compd.* **2015**, *618*, 248−253.
(27) Bishop, D. M.; McCandless, B.; Gershon, T.; Lloyd, M. A.; Haight, R.; Birkmire, R. Modification of Defects and Potential Fluctuations in Slow-Cooled and Quenched $Cu_2ZnSnSe_4$ Single Crystals. *J. Appl. Phys.* **2017**, *121*, 065704.
(28) Simonsen, S. B.; Chorkendorff, I.; Dahl, S.; Skoglundh, M.; Sehested, J.; Helveg, S. Direct Observations of Oxygen-Induced Platinum Nanoparticle Ripening Studied by in Situ TEM. *J. Am. Chem. Soc.* **2010**, *132*, 7968−7975.
(29) Yu, P. W. Excitation-Dependent Emission in Mg^-, Be^-, Cd^-, and Zn^- Implanted GaAs. *J. Appl. Phys.* **1977**, *48*, 5043−5051.
(30) Campbell, S.; Qu, Y.; Bowen, L.; Chapon, P.; Barrioz, V.; Beattie, N. S.; Zoppi, G. Influence of OLA and FA Ligands on the Optical and Electronic Properties of $Cu_2ZnSn(S,Se)_4$ Thin Films and Solar Cells Prepared from Nanoparticle Inks. *Sol. Energy* **2018**, *175*, 101−109.
(31) Tiwari, D.; Skidchenko, E.; Bowers, J. W.; Yakushev, M. V.; Martin, R. W.; Fermin, D. J. Spectroscopic and Electrical Signatures of Acceptor States in Solution Processed $Cu_2ZnSn(S,Se)_4$ Solar Cells. *J. Mater. Chem. C* **2017**, *5*, 12720−12727.
(32) Raadik, T.; Krustok, J.; Kauk-Kuusik, M.; Timmo, K.; Grossberg, M.; Ernits, K.; Bleuse, J. Low Temperature Time Resolved Photoluminescence in Ordered and Disordered Cu_2ZnSnS_4 Single Crystals. *Phys. B* **2017**, *508*, 47−50.

DOI: 10.1021/acsaem.9b01732
ACS Appl. Energy Mater. 2020, 3, 122−128